JOURNAL OF EXPERIMENTAL AND THEORETICAL PHYSICS, 2025, Vol. 167, No. 1, pp. 64–75

SOLIDS AND LIQUIDS

NEUTRON CHANNELING IN A MAGNETIC PLANAR WAVEGUIDE

© 2025 S. V. Kozhevnikov[a,*], Yu. N. Khaydukov[b, c, d]

[a]Frank Laboratory of Neutron Physics, Joint Institute for Nuclear Research, Dubna, Moscow region, Russia
[b]Skobeltsyn Institute of Nuclear Physics Lomonosov Moscow State University, Moscow, Russia
[c]Max Planck Institut für Festkörperforschung, Stuttgart, Germany
[d]Max Planck Society Outstation at FRM–II, Garching, Germany
*e-mail: kozhevn@nf.jinr.ru

Received May 08, 2024

Reveised June 03, 2024

Accepted June 10, 2024

Abstract. Tri-layered waveguide transforms a conventional collimated neutron beam into a narrow divergent microbeam. Propagation of neutrons in a waveguide with enveloping magnetic layers is investigated. Intensity of the neutron microbeam emitted from the end face of the nonmagnetic middle layer is registered. Neutron channeling length is defined experimentally in dependence on the sign of polarization of the incident beam.

Keywords: *layered nanostructures, neutron resonators, waveguides, neutron channeling, neutron microbeam*

DOI: 10.31857/S00444510250106e6

1. INTRODUCTION

Neutron scattering is a powerful non-destructive method for studying magnetic structures, polymers, and biological objects due to the unique properties of neutrons: the presence of an intrinsic magnetic moment, high penetrating ability, and isotopic sensitivity. The properties of neutron and X-ray radiation differ significantly, making them complementary methods. For example, polarized neutron beams are a unique tool for studying magnetic materials within the bulk of a substance, which is inaccessible to X-rays due to their low penetrating ability.

The width of the neutron beam determines the spatial resolution and the scale of the studied objects. The typical beam width in neutron experiments ranges from 0.1 to 10 mm. To study local microstructures on the scale of tens of micrometers, very narrow neutron beams are required. For this purpose, various focusing devices are being developed (parabolic mirror neutron guides, refractive lenses, curved monochromator crystals, etc.) [1], capable of compressing the neutron beam to 50 μm. Achieving a smaller beam width is hindered by limitations imposed by the physical properties of the materials used and the technology of their processing. Another problem with these devices is their inability to effectively isolate a "pure" microbeam. For example, parabolic mirror neutron guides form a highly structured beam in space, refractive lenses focus only 20–30% of the initial beam, and capillary lenses generate significant background noise.

In [2], the profile of a microbeam after passing through an aperture formed by neutron-absorbing crystal blades $Gd_2Ga_5O_{12}$ (or GGG) was calculated. The resulting microbeam had a central part about 100 μm wide and wings ranging from 10 to 20 μm. The study also demonstrated a method for obtaining a microbeam through total reflection of neutrons from a silicon substrate. This method has undeniable advantages: high intensity (~1000 neutrons/s), low background (~2 neutrons/min), and compatibility with time-of-flight techniques. However, the practically achievable microbeam width at a neutron wavelength of 4.0 Å and an 8 mm wide silicon substrate still remains around 30 μm.

The record holders for the minimum width of neutron microbeams are triple-layer waveguides (Fig. 1). Their operating principle is as follows. A collimated neutron beam with an angular divergence $\delta\alpha_i$ falls in a vacuum (medium 0) onto the surface of the waveguide at a small grazing

angle α_i. The neutrons then tunnel through a thin upper layer (medium 1) with a thickness of $a = 5-20$ nm and enter the middle layer (medium 2) with d=100–200 nm. They are almost completely reflected from the relatively thick lower layer (medium 3), deposited on a thick substrate (e.g., glass). Some of the neutrons tunnel back through the upper layer and exit the waveguide as a reflected beam $\alpha_f = \alpha_i$. Another portion of the neutrons reflects from the upper thin layer 1 and returns to the middle layer 2. As a result of multiple reflections, the neutrons propagate along the middle layer as if through a channel and exit from its end as a microbeam with an angular divergence $\delta\alpha_f$. The main contribution to the angular divergence $\delta\alpha_f$ of the microbeam comes from Fraunhofer diffraction $\delta\alpha_F$ at the narrow slit d formed by the waveguide channel $\delta\alpha_F \propto \lambda / d$, where λ is the neutron wavelength.

Layered neutron waveguides have been well studied to date. In [3], an unpolarized neutron microbeam was obtained from the end of a triple-layer waveguide, while in [4], a polarized beam was achieved. The contribution of Fraunhofer diffraction $\delta\alpha_F$ to the angular divergence of the neutron microbeam was experimentally determined in [5, 6, 7]. In [2, 8], a polarized neutron microbeam from a waveguide was used for spatial scanning of a 190 μm diameter microwire made of amorphous magnetic material. At a distance of 1 mm from the waveguide exit, with a neutron wavelength of 4.0 Å, a waveguide channel width of 150 nm, and an angular divergence 0.15°, the calculated microbeam width at the sample location was 2.6 μm. With a microbeam intensity of approximately 1 neutron/s, statistically significant data were obtained within about 10 hours. The experimental setup is described in detail in [2]. The advantages of planar waveguides include the record-low width of the neutron microbeam and a relatively simple method for separating the microbeam from the background. Their obvious disadvantages are low intensity and relatively high beam divergence. However, the commissioning of more powerful neutron sources (SNS, ESS, PIK, IBR-3) may make the use of layered waveguides more accessible.

In planar waveguides, two phenomena are observed simultaneously – resonant enhancement of neutron standing waves and neutron channeling. The theory of neutron resonances in layered waveguides is described in [9]. Let us introduce the following notations:

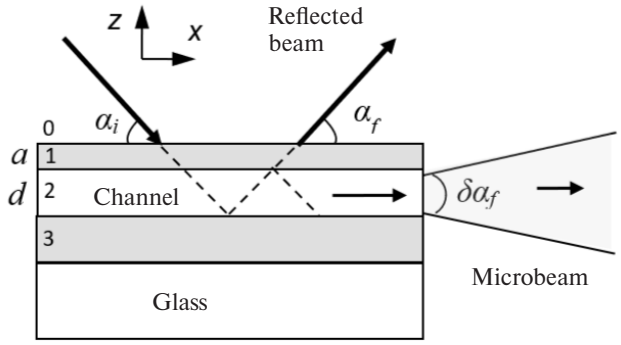

Fig. 1. Principle of operation of a planar neutron waveguide

$$k_{0z} = \frac{2\pi}{\lambda}\sin\alpha_i,$$

$$k_{1z} = \sqrt{k_{0z}^2 - \rho_1}, \quad k_{2z} = \sqrt{k_{0z}^2 - \rho_2},$$

$$k_{0x} = \frac{2\pi}{\lambda}\cos\alpha_i.$$

Here, ρ_1 is the neutron scattering length density (SLD) for the upper layer 1, and ρ_2 is the SLD for the waveguide layer 2. The general form of the neutron wave function is given by:

$$\Psi(k_{0z}, z) = A\exp(ik_{0z}z),$$

where A is the amplitude of the wave function. Then, we obtain the condition $|\Psi|^2 = |A|^2$. Inside the middle layer, the wave function takes the form:

$$\Psi(z) = A\left[\exp(-ik_{2z}z) + R_{23}\exp(ik_{2z}z)\right],$$

where R_{23} is the amplitude of the reflected neutron wave function from the lower layer 3. The amplitude A is determined from the self-consistent equation for the neutron wave function in layer 2, if the origin z=0 is aligned with the boundary between layers 1 and 2:

$$A = T_{02}\exp(ik_{2z}d) + R_{21}R_{23}\exp(ik_{2z}2d)A, \quad (1)$$

where T_{02} is the amplitude of the transmitted neutron wave function from vacuum (medium 0) into medium 2, and R_{21} is the amplitude of the reflected neutron wave function in medium 2 from layer 1. From the self-consistent equation (1), we find:

$$|\Psi|^2 = |A|^2 = \frac{|T_{02}|}{|1 - R_{21}R_{23}\exp(2ik_{2z}d)|}. \quad (2)$$

The quantity $|A|^2$ in equation (2) exhibits resonant maxima under the periodic conditions for the phase of the neutron wave function:

$$\Phi(k_{0z}) = 2k_{2z}d + \arg(R_{21}) + \arg(R_{23}) = 2\pi n, \quad (3)$$

where $n = 0,1,2,\ldots$ is the resonance order. If the neutron wavelength is fixed, the grazing angle of the incident beam has resonances depending on the angle α_{in}. If the time-of-flight method is used, the grazing angle is fixed, and the final neutron spectrum exhibits resonances depending on the wavelength λ_n. In [10], it was experimentally shown using a time-of-flight reflectometer that the spectral width of neutron resonances increases with the divergence $\delta\alpha_i$ of the incident beam.

The parameter $|A|^2$ represents the neutron density enhancement coefficient inside the middle layer, and for various resonators, it can reach values of the order of 10^1–10^3. Layered resonators are used to amplify the weak interaction of neutrons with matter [11]. Neutron resonances appear as weak minima in the coefficients of neutron specular reflection and as corresponding resonance-enhanced maxima of secondary characteristic radiation or specific neutron scattering. During neutron interactions with certain elements and isotopes, secondary characteristic radiation, such as gamma rays [12] and alpha particles [13], is generated due to nuclear reactions. The experimental setup and the method of neutron reflectometry with the detection of secondary radiation are described in detail in [14–17].

Specific neutron scattering within the resonator can also include neutrons that experience spin-flip interactions with magnetically non-collinear layered structures [18, 19, 20], incoherent scattering from hydrogen [21], and off-specular scattering from interlayer roughness [22, 23] and domain structures [24, 25]. The high sensitivity of neutron resonance positions to changes in the SLD of the resonant layer has been utilized to detect small variations in hydrogen concentration within the resonator [26, 27]. These resonators can be applied as sensors in hydrogen storage systems.

Another type of specific neutron scattering is neutron channeling. A neutron beam propagating along the middle layer can exit through the waveguide surface as a collimated beam of standard width or from the channel end as a narrow divergent microbeam (see Fig. 1). The intensities of both neutron beams exhibit resonance maxima depending on energy. In [28], the idea of using planar neutron waveguides to determine weak magnetization of films on the order of 10^2 G was proposed. This idea was experimentally implemented in [29] and [30]. In the three-layer waveguide, the outer layers were non-magnetic, while the investigated ferrimagnetic films $TbCo_5$ [29] and $TbCo_{11}$ [30] acted as the middle waveguide layer. The magnetization value is determined directly from the difference in the resonance positions, which varies by about n=0 for the incident beam polarizations "+" and "–". Moreover, registering the microbeam allows effective separation of the useful signal from the background, originating from the specularly reflected, refracted, and bypassing beams. In this study, we examine a waveguide where the outer layers are magnetic and the middle layer is non-magnetic (see Fig. 2). In such waveguides, the neutron density enhancement coefficient within the waveguide channel depends on the neutron spin projection "+" or "–" relative to the magnetization vector direction. In [31], the idea was proposed to control the chain reaction of uranium fission within the non-magnetic waveguide layer by magnetizing the outer layers using an applied magnetic field. This approach alters the parameter x_e, which characterizes the exponential attenuation of the neutron density, known as the channeling length.

In [32], it was theoretically demonstrated that during neutron propagation along the waveguide channel, the neutron wavefield attenuates as $\exp(-x / x_e)$, where x is the distance under the unilluminated surface of the waveguide. The expression for the neutron channeling length was derived as:

$$x_e = \frac{k_x d}{k_{2z}\left|\ln\left|R_{21}R_{23}\right|\right|}. \quad (4)$$

If the lower layer is sufficiently thick, we can assume $R_{23} = 1$. If the neutron reflection amplitude from the upper layer is close to unity $R_{21} \approx 1$, the neutron transmission coefficient through the upper layer becomes a small parameter:

$$T = |T_{20}| = 1 - |R_{21}|$$

Thus, we can write an approximate expression:

$$\left|\ln\left|R_{21}R_{23}\right|\right| \approx \left|\ln(1-T)\right| \approx T.$$

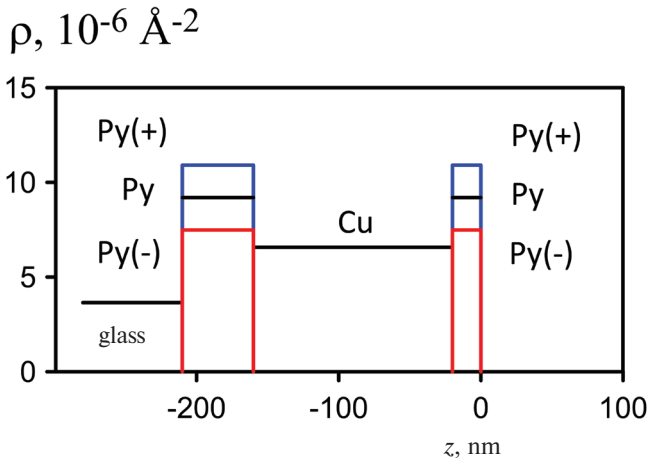

Fig. 2. Neutron scattering length density (SLD) of the waveguide with magnetic outer layers as a function of the coordinate z perpendicular to the layers. The notation Py(+) corresponds to the polarization "+" and a film magnetization of 7.2 kG, Py (—) corresponds to the polarization "–" and a film magnetization of 7.2 kG, while Py represents the unpolarized beam and the demagnetized sample.

In this case, we obtain a simplified expression for the neutron channeling length:

$$x_e \approx \frac{k_x d}{k_{2z} T}. \qquad (5)$$

The neutron channeling length can be determined experimentally. A strip of neutron-absorbing material is applied near the exit edge of the waveguide, creating an unilluminated region of length x. Then, by varying the absorber's position and changing the length of the unilluminated region x, the intensity $I(x)$ of the microbeam emerging from the waveguide end is measured. For normalization, the microbeam intensity without the absorber $I(x = 0)$ is recorded.

According to the channeling theory [32], the intensity of the neutron microbeam from the waveguide channel end attenuates exponentially with increasing length of the unilluminated waveguide surface:

$$I(x) / I(x = 0) = \exp(-x / x_e). \qquad (6)$$

From the experimental dependence of the microbeam intensity (6), the neutron channeling length x_e can be determined. For various waveguides, this value typically ranges between 0.5 and 5.0 mm.

Various materials are used as neutron absorbers: Gd_2O_3 powder, Cd plates, or boral (an aluminum-boron carbide composite) bars. Fig. 3 shows the

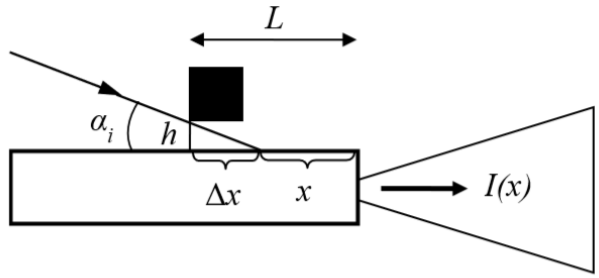

Fig. 3. Experimental setup for determining the neutron channeling length using a sliding absorber bar.

experimental setup with a sliding boral block. Due to the block's curvature, an air gap of approximately with $h \approx 10\mu m$ forms between the block and the waveguide surface. As a result, part of the waveguide surface under the absorber, with a length Δx of about 1.5 mm, remains illuminated by the incident neutron beam. In the experiment, the intensity $I(L)$ of the neutron microbeam is recorded as a function of the distance L from the waveguide exit edge to the front edge of the absorber. The coordinate $L = \Delta x + x$ includes both the illuminated length Δx and the unilluminated length x of the waveguide surface under the absorber. By transforming the coordinates, the dependence of the microbeam intensity on the unilluminated surface length $x = L - \Delta x$ is determined. The intensity $I(x)$ of the microbeam with the fully illuminated waveguide surface $I(x = 0)$ is used for normalization. The value Δx not need to be known in advance; it is determined automatically during the data processing, described in detail in Section 3.

The experimental setup and various methods for measuring the neutron channeling length are presented in [33]. Two neutron absorbers were compared: a sliding boral block and Gd_2O_3 powder. The advantage of the powder lies in its low background in the microbeam and simpler data processing, as there is no air gap between the surface and the powder. However, the drawbacks of the powder include: 1) significant time consumption when changing the absorber width; 2) practical infeasibility for neutron channeling lengths shorter than 1 mm;

The advantages of the sliding boral block are: 1) precise position control using a micrometer screw; 2) faster repositioning compared to the powder absorber; 3) suitability for determining short channeling lengths less than 1 mm. The drawbacks of the sliding boral block are higher background levels

in the microbeam compared to the powder absorber and more complex data processing.

The same study [33] experimentally demonstrated that the exponential attenuation parameter of neutron density in the reflection geometry is smaller than the channeling length in the microbeam geometry from the waveguide end.

The phenomenon of neutron channeling in three-layer waveguides was first observed in the reflection geometry in [34]. The first experimental measurement of the neutron channeling length in the microbeam geometry was performed in [35] using an absorbing powder on the surface. In [36], experiments were conducted with a Cd plate on the sample surface. A comprehensive review of studies on planar neutron waveguides is provided in [37], showing that the channeling length (5) depends on the resonance order $n = 0,1,2\ldots$ and the waveguide parameters – upper layer thickness a, channel width d, and the depth of the potential well defined by the scattering length density (SLD) contrast $\Delta\rho = \rho_1 - \rho_2$.

The following relationships were derived for the resonance order $n = 0$:

$$\ln x_e \propto a, \quad \ln x_e \propto d, \quad \ln x_e \propto \Delta\rho$$

and the first three resonance orders $n = 0, 1, 2$:

$$x_e \propto 1/(n+1)$$

Experiments with the sliding boral block determined the neutron channeling length as a function of resonance order and upper layer thickness [38], waveguide channel width [39], and potential well depth for various waveguides [40]. The experimental results confirmed theoretical predictions.

In this study, we experimentally determine the neutron channeling length in a waveguide with magnetic outer layers, where the potential well depth varies depending on the neutron beam polarization.

2. CALCULATIONS

Calculations were performed for the Py(20 nm)/Cu(140 nm)/Py(50 nm)//glass waveguide. Permalloy (Py) is a magnetic Fe(20.6 at.%)Ni(79.4 at.%) alloy with a narrow hysteresis loop. Figure 2 shows the neutron scattering length density (SLD) profile of the waveguide as a function of the coordinate z perpendicular to the layers. The designations Py(+) and Py(–) correspond to the SLD of saturated permalloy for neutron spins "UP" and "DO," respectively, while Py represents the SLD for the fully demagnetized state of permalloy. As seen in the figure, the SLD of permalloy changes depending on the neutron spin direction. The permalloy magnetization used for calculations is 7.2 kG, and the neutron wavelength is 4.26 Å. Fig. 4 presents the calculated squared modulus of the neutron wavefunction $|\Psi|^2$ as a function of the incident beam's grazing angle α_i and the coordinate z perpendicular to the layers. Fig. 4a shows "+" polarization, Fig. 4b shows calculations for the unpolarized NM beam, while Fig. 4c shows "–" polarization. Resonances of orders $n = 0,1,2\ldots$,... are visible, with the most intense ones located within the total reflection region below the horizontal dashed line. The neutron density enhancement coefficient reaches 30 for the UP polarization and the $n = 0$ resonance. Notably, the two-dimensional neutron density maps differ depending on the neutron beam polarization. As the waveguide potential well depth decreases, the resonance positions shift to lower incident angles, the distance between resonances decreases, and the resonance peak intensities also decrease.

Fig. 5a shows the neutron specular reflection coefficients for the UP polarization (thin line), the unpolarized NM beam (dashed line), and the DO polarization (thick line) as a function of the incident beam's grazing angle. It is evident that the total reflection region shifts toward smaller grazing angles for the NM and DO polarizations compared to the UP polarization. Additionally, minima in the reflection coefficients appear in the total reflection region, corresponding to resonance conditions $n = 0,1,2\ldots$.

In Fig. 5b, the square modulus of the neutron wavefunction $|\Psi|^2$ (in relative units), integrated over the coordinate z within the waveguide channel, is shown as a function of the incident beam's grazing angle. Resonance peaks $n = 0,1,2\ldots$ corresponding to the resonance order are clearly visible. If the peak value for the $n = 0$ resonance with UP polarization is normalized to 1.0, the corresponding peak for the unpolarized beam is 0.8, while for DO polarization it is 0.4. Thus, the square modulus of the neutron wavefunction $|\Psi|^2$ depends significantly on the potential well depth of the waveguide.

Fig. 6 shows the neutron channeling length $n = 0$ resonance as a function of the waveguide's potential

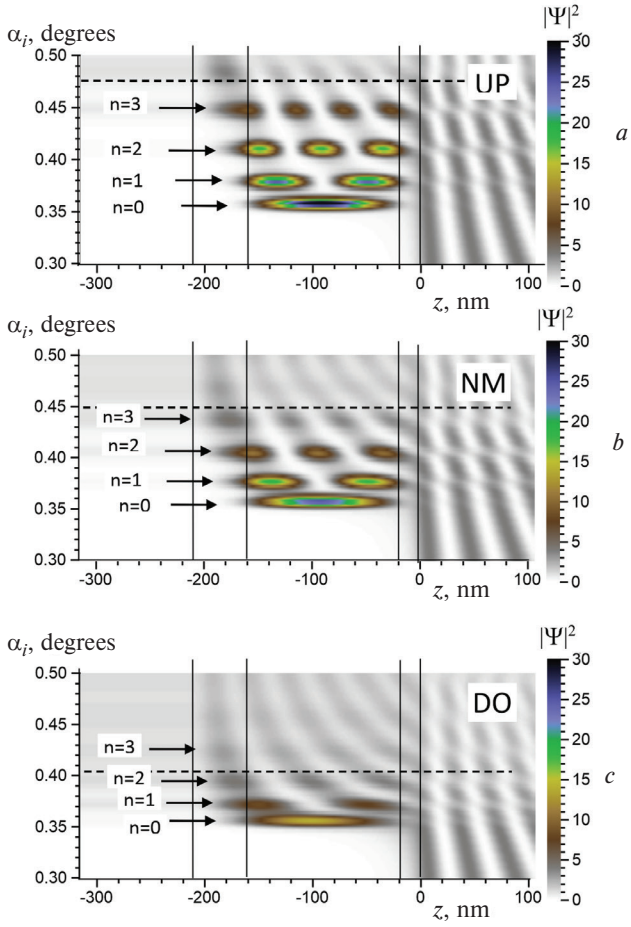

Fig. 4. Calculated squared modulus of the neutron wavefunction as a function of the grazing angle of the incident beam and the coordinate perpendicular to the layers for different initial beam polarizations: (a) UP; (b) Unpolarized NM beam; (c) DO. Neutron wavelength: 4.26 Å.

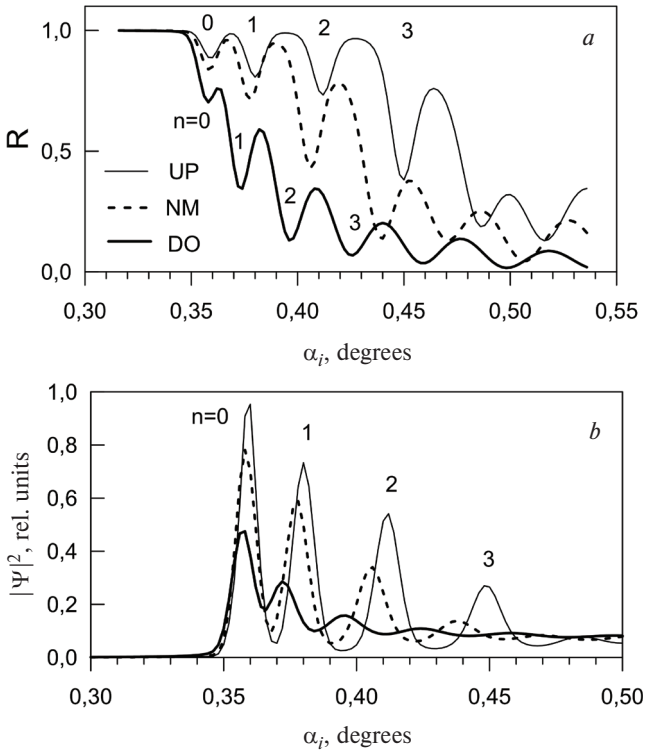

Fig. 5. Calculations: (a) Neutron specular reflection coefficient for UP polarization (thin line), DO polarization (thick line), and unpolarized NM beam (dashed line) as a function of the incident beam's grazing angle. (b) Square modulus of the neutron wavefunction for UP and DO polarizations and for the unpolarized NM beam as a function of the incident beam's grazing angle.

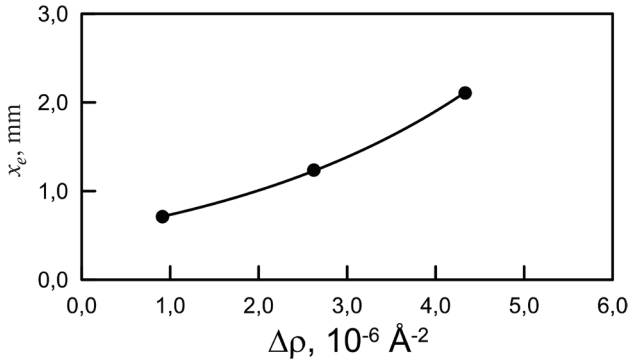

Fig. 6. Calculated neutron channeling length as a function of the waveguide potential well depth for different incident beam polarizations.

well depth, calculated for a neutron wavelength of 4.26 Å using Equation (5). The dots represent the calculated data, while the solid line represents an exponential fit. It is evident that the neutron channeling length increases exponentially with increasing waveguide potential well depth. Thus, preliminary calculations predict an exponential growth of both the square modulus of the neutron wavefunction and the neutron channeling length as the waveguide potential well depth increases.

3. EXPERIMENT

The experiments were conducted on the NREX polarized neutron reflectometer (FRM II reactor, Garching, Germany) [41]. The sample plane was positioned horizontally, allowing the boral block absorber to rest freely on the waveguide surface. The dimensions of the Py(20 nm)/Cu(140 nm)/Py(50 nm)//glass sample substrate were $30 \times 30 \times 5\ \text{mm}^3$, while the absorber block dimensions were $1 \times 1 \times 38\ \text{mm}^3$. The neutron wavelength was 4.26 Å. In polarized beam mode, the wavelength resolution was 1.5%, and the incident beam divergence was 0.006°. The angular resolution of the

^{3}He two-dimensional position-sensitive detector was 0.072°.

The polarization efficiency of the single supermirror polarizer was 97%, and it was used in the transmission geometry. An external magnetic field of 1.0 kOe was applied parallel to the sample plane to magnetize the permalloy films to saturation. The first aperture width was 0.25 mm, with a distance of 2200 mm from the first aperture to the sample and 2400 mm from the sample to the detector. The detector's spatial resolution was 3.0 mm. A second aperture, 0.7 mm wide, was placed 200 mm before the sample to reduce background noise.

The demagnetized state of the sample was achieved by applying an external magnetic field of +3 Oe along the film plane. This field value was determined from the hysteresis loop measured using the degree of polarization of the specularly reflected beam. During the determination of the neutron channeling length in the demagnetized waveguide, the unpolarized beam mode was used, with the polarizer removed from the beam path. The first aperture width was 0.35 mm, the neutron wavelength resolution was 2.0%, and the incident beam divergence was 0.009°.

Fig. 7a presents the neutron specular reflection coefficients for "+" polarization (light points) and "–" polarization (dark points) as a function of the incident beam's grazing angle. The solid lines show the fit results with the following parameters: layer thicknesses (nm), nuclear SLD (Å^{-2}), and magnetization of the layers (kG).

$$\text{PyO}(2.3\ \text{nm}, 7.67\cdot10^{-6}\ \text{Å}^{-2})/$$

$$/\text{Py}(19.5\ \text{nm}, 8.83\cdot10^{-6}\ \text{Å}^{-2}, 7.0\ \text{kG})/$$

$$/\text{Cu}(132.0\ \text{nm}, 6.58\cdot10^{-6}\ \text{Å}^{-2})/$$

$$/\text{Py}(48.0\ \text{nm}, 8.56\cdot10^{-6}\ \text{Å}^{-2}, 7.2\ \text{kG})//$$

$$//\text{glass}\ (2.63\cdot10^{-6}\ \text{Å}^{-2}).$$

The fit results indicate that the magnetization of the upper permalloy layer is 7.0 kG, while the magnetization of the lower layer is 7.2 kG. Fig. 7b shows the specular reflection coefficient for the unpolarized neutron beam reflected from the demagnetized sample. The fit with zero magnetization of the permalloy layers accurately describes the experimental data.

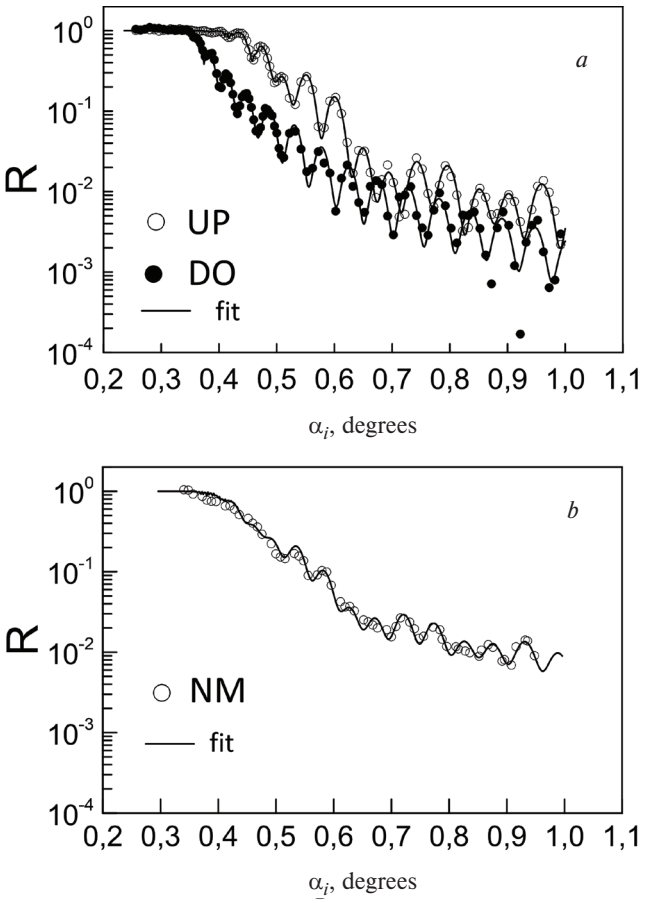

Fig. 7. Neutron specular reflection coefficients as a function of the incident beam's grazing angle (dots – experiment, lines – fit): (a) polarized beams UP and DO; (b) unpolarized beam NM.

Fig. 8a displays the neutron microbeam intensity without an absorber on the waveguide surface as a function of the incident beam's grazing angle for the initial polarizations "+" (light symbols) and "–" (dark symbols) with the fully illuminated waveguide surface. The resonance peaks are labeled with the corresponding resonance orders $n = 0, 1, 2\ldots$.

It can be seen that the microbeam intensity peak at the $n = 0$ resonance (background-subtracted) for the initial "–" polarization is approximately twice lower than the peak intensity for the "+" polarization. Higher-order resonances ($n = 1, 2, 3$) are clearly visible for the "+" polarization. For the "–" polarization, only a small peak at the $n = 1$ resonance is observed, significantly shifted to lower incident angles compared to the $n = 1$ resonance for the "+" polarization. The intensity of higher-order resonances for the "–" polarization is low, making the corresponding peaks barely visible.

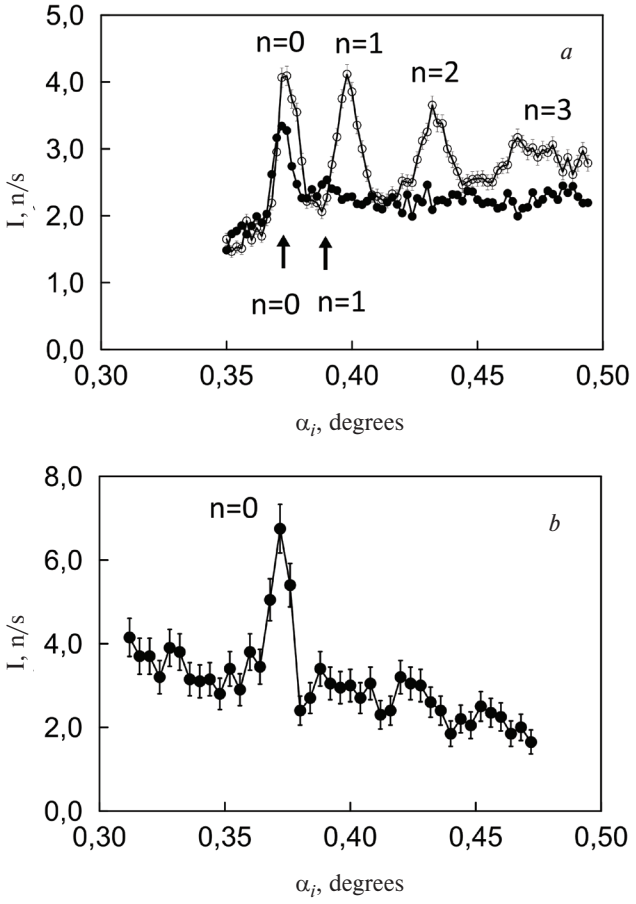

Fig. 8. Neutron microbeam intensity as a function of the incident beam's grazing angle: (a) incident beam polarization UP (light symbols) and DO (dark symbols); (b) unpolarized beam.

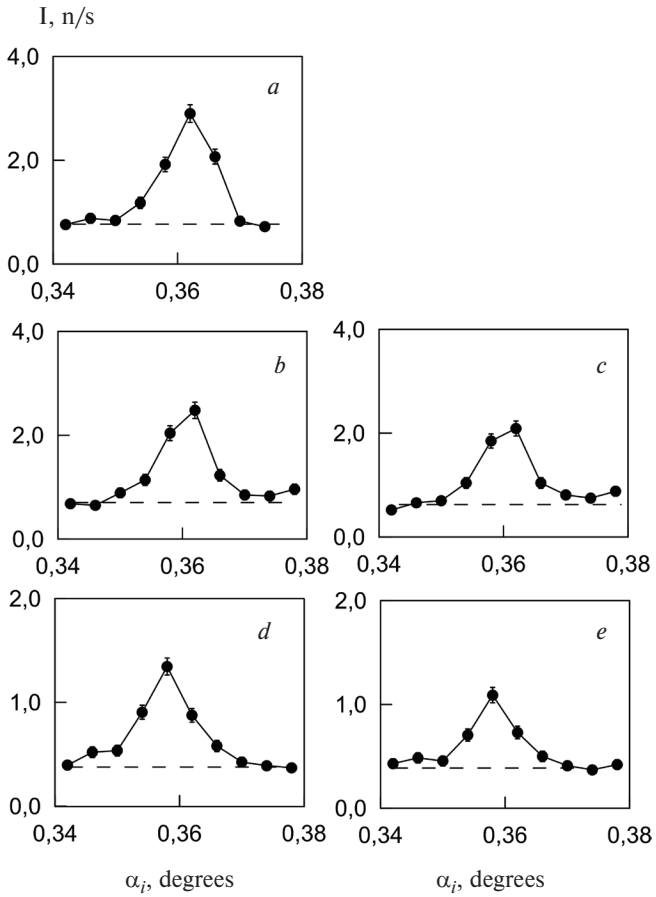

Fig. 9. Microbeam intensity for UP polarization as a function of the incident beam's grazing angle at different distances L between the front edge of the absorber on the surface and the output edge of the waveguide: (a) 1.0 mm; (b) 1.5 mm; (c) 2.5 mm; (d) 3.5 mm; (e) 4.0 mm. The dashed line indicates the background level. Data obtained from [38].

Fig. 8b shows the neutron microbeam intensity without an absorber on the surface of the demagnetized sample as a function of the incident angle of the unpolarized neutron beam. The peak corresponding to the $n = 0$ resonance is clearly visible. For normalization, the microbeam intensity $I(x = 0)$ is measured with the absorber placed at the very edge of the waveguide exit, when the waveguide surface is fully illuminated by the incident neutron beam. In this case, the main part of the specularly reflected beam is blocked by the absorber, reducing the background level near the microbeam by approximately 50%. This position corresponds to an absorber offset of $L = 1.0\,\text{mm}$ relative to the waveguide exit edge.

Fig. 9 presents the neutron microbeam intensity as a function of the grazing angle of the incident UP-polarized beam for different absorber positions relative to the waveguide exit edge: 1.0, 1.5, 2.5, 3.5, and 4.0 mm. These data were obtained and published in our previous work [38]. As the absorber moves away from the waveguide edge, the neutron microbeam intensity decreases systematically.Further studies were conducted on the demagnetized sample. Fig. 10 shows the intensity of the neutron microbeam as a function of the grazing angle of the incident unpolarized neutron beam (NM) for the absorber block positioned relative to the waveguide's output edge at 1.0, 2.3, and 2.7 mm. It can be observed that the microbeam intensity decreases as the distance from the waveguide's output edge to the absorber's front edge increases.

Fig. 11 presents the neutron microbeam intensity as a function of the grazing angle of the incident polarized DO beam for different absorber positions relative to the waveguide's output edge: 1.0, 1.7, 1.9, 2.2, and 2.4 mm. As seen, the microbeam

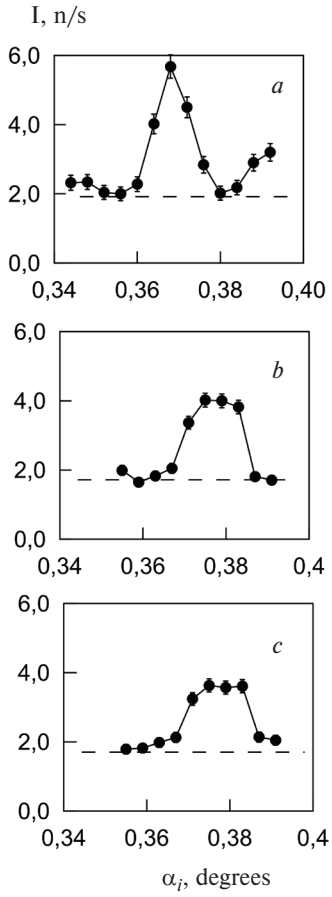

Fig. 10. Microbeam intensity in the unpolarized mode as a function of the incident beam's grazing angle at different distances L between the front edge of the absorber on the surface and the output edge of the waveguide: (a) 1.0 mm; (b) 2.3 mm; (c) 2.7 mm. The dashed line indicates the background level.

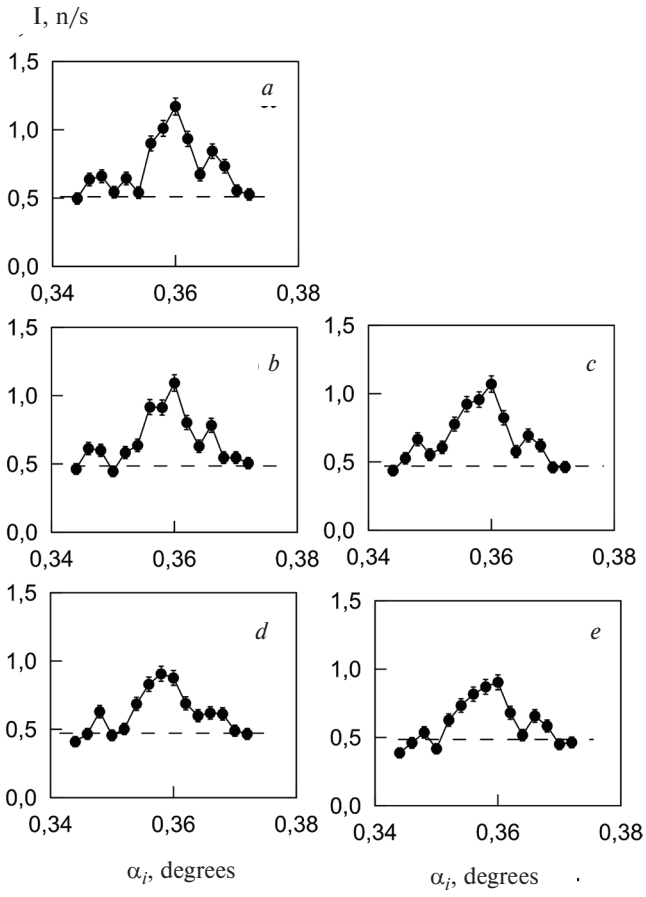

Fig. 11. Microbeam intensity for DO polarization as a function of the incident beam's grazing angle at different distances L between the front edge of the absorber on the surface and the output edge of the waveguide: (a) 1.0 mm; (b) 1.7 mm; (c) 1.9 mm; (d) 2.2 mm; (e) 2.4 mm. The dashed line indicates the background level.

intensity decreases with increasing distance from the waveguide output to the front edge of the absorber block.

Fig. 12 displays the normalized neutron microbeam intensity $I(L)/I(x=0)$ on a natural logarithmic scale as a function of the distance L from the waveguide's output edge to the absorber block's front edge (upper scale and light symbols) for the incident polarized UP beam (a), the unpolarized NM beam and demagnetized sample (b), and the polarized DO beam (c). The condition $I(L=1\,\text{mm}) = I(x=0)$ is taken into account.

It can be observed that the experimental points for $L > 1$ mm align along a straight line intersecting the 1.00 level at L. Vertical error bars represent statistical uncertainties in the neutron microbeam intensity. The data processing is performed as follows: the normalized intensity point at $L = 1$ mm is placed at the origin ($x = 0$) on the horizontal axis. Subsequently, all remaining points along the L coordinate (light symbols) are shifted by a single value L along the horizontal axis so that the line through all $x = L - L'$ coordinate points (dark symbols and lower scale) passes through the origin $x = 0$. The shift value L' depends on the accuracy of the initial absorber block positioning relative to the waveguide's output edge and the size of the air gap between the absorber and the waveguide surface. Consequently, the line $\ln[I(x)/I(x=0)] = -x/x_e$ intersects the 0.37 level on the vertical axis at the point corresponding to the experimental neutron channeling length. The uncertainty in the neutron channeling length is determined by the extreme trajectories passing through the experimental points, considering the statistical error of the microbeam intensity. It is noteworthy that the longest neutron channeling length is observed for the UP-polarized incident

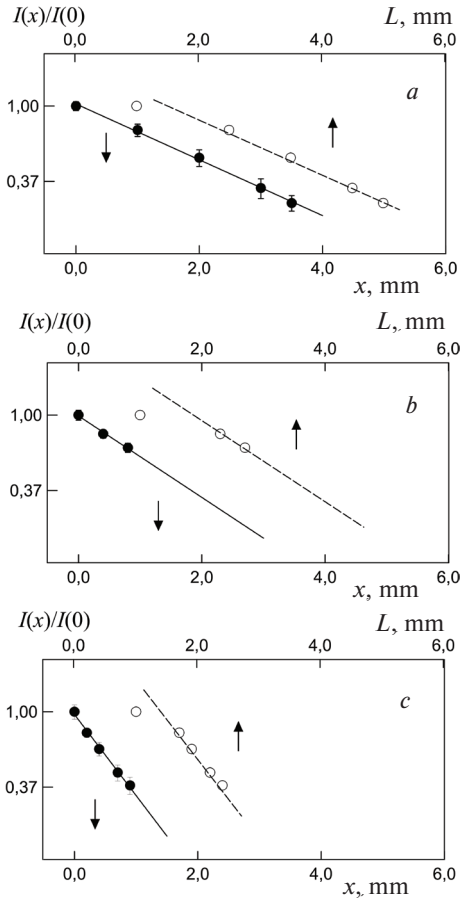

Fig. 12. Normalized microbeam intensity on a natural logarithmic scale as a function of the distance L from the output edge of the waveguide to the front edge of the absorber block (upper scale and light symbols) and the length of the non-illuminated surface area of the waveguide x (lower scale and dark symbols) for different polarization values: (a) UP, (b) NM, (c) DO.

beam (Fig. 12a). The channeling length decreases for the unpolarized NM beam and the demagnetized sample (Fig. 12b). The shortest channeling length is observed for the DO polarization (Fig. 12c).

The illuminated surface area under the absorber Δx in Fig. 3 corresponds to the point L' when the absorber block just begins to partially cover the waveguide surface from the incident beam. From the equality $\Delta x = L'$, the air gap under the block can be estimated as $h \approx \alpha_i \Delta x$.

Fig. 13 shows the experimental neutron channeling length as a function of the waveguide's scattering length density (SLD) depth $\Delta\rho = \rho_1 - \rho_2$. The points represent the experimental data, while the line represents the least-squares exponential fit. It is evident that the experimental data follow an exponential dependence, qualitatively confirming

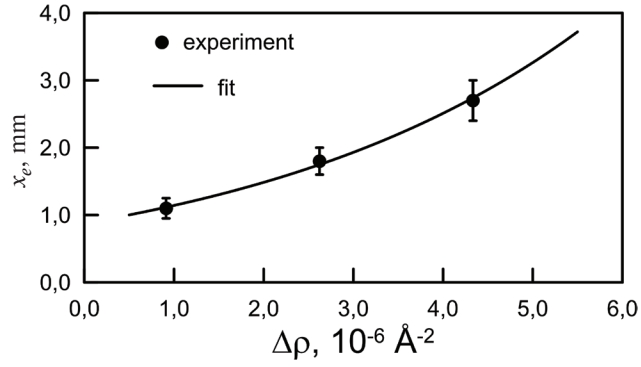

Fig. 13. Neutron channeling length as a function of the waveguide's SLD depth for different incident beam polarizations. Points represent experimental data, and the line represents the least squares exponential fit.

the preliminary channeling theory calculations. The quantitative comparison between theory and experiment depends on the precise determination of the actual structural parameters (oxide layer thickness, layer thicknesses, SLD, and layer magnetization). However, minor deviations of the experimentally obtained structure parameters from nominal values should not affect the overall trend of the neutron channeling length's dependence on the waveguide potential well depth. The channeling theory was previously validated experimentally [35]. The calculated neutron channeling length, with refined Fe/Cu/Fe//glass waveguide parameters, matched the experimentally obtained value within statistical error limits.

4. DISCUSSION OF RESULTS

The examined magnetic waveguide Py/Cu/Py can be utilized in two directions. First, as a polarizer for generating a polarized neutron microbeam in experiments studying magnetic microstructures. From the intensity ratio of the UP and DO microbeam polarizations for the resonance of order $n = 0$ (see Fig. 8a), it follows that the waveguide's polarization efficiency is 0.3. The review [37] provides a detailed discussion of various polarizing and non-polarizing magnetic waveguides. For example, the Fe(20 nm)/Cu(140 nm)/Fe(50 nm)// glass waveguide has a polarization efficiency of 0.6 for the $n = 0$ resonance. The polarization efficiency of the magnetic waveguide Fe(20 nm)/Co(150 nm)/ Fe(50 nm)//Si reaches 1.0.

Magnetic waveguides have a significant drawback. Due to the high divergence of the microbeam, the

sample under study must be located approximately 1 mm from the waveguide's exit. In such an experimental setup, it is challenging to separate the magnetic field on the waveguide from the field on the sample. The most practical solution is a combination of a polarized neutron reflectometer and a non-magnetic waveguide [42]. In this configuration, high polarization of the microbeam is achieved conventionally, and the magnetic field on the sample does not affect the operation of the non-magnetic waveguide. This non-magnetic waveguide setup was used in the experiment with the magnetic microwire [2, 8]. Thus, non-magnetic waveguides have an advantage over magnetic ones in experiments studying magnetic microstructures using polarized neutron microbeams.

The second application of magnetic neutron waveguides is for controlling the chain reaction of uranium fission. The idea proposed in [31] suggests that by remagnetizing the external magnetic layers with an applied magnetic field, the neutron density in the middle non-magnetic layer can be altered. If uranium is placed inside the non-magnetic layer, the uranium fission reaction can be controlled using an external magnetic field. Suitable candidates for this method include the Py/Cu/Py and Fe/Cu/Fe magnetic waveguides. The preferred choice is the Fe/Cu/Fe waveguide, which has twice the polarization efficiency. However, in this study, we investigated the Py/Cu/Py waveguide. For the DO polarization of the incident beam, the waveguide retains a shallow potential well of the scattering length density (SLD), enabling experimental measurement of the neutron channelling length for this polarization. Clearly, non-magnetic waveguides are not suitable for controlling the chain reaction, as they do not respond to the magnetic field.

5. CONCLUSION

This study investigated the Py/Cu/Py//glass neutron waveguide with external magnetic layers. The magnitude of the SLD of the magnetic layer depends on the sign of the incident neutron beam polarization. Preliminary calculations based on the theory of resonances in layered nanostructures showed that the square of the neutron wave function modulus inside the waveguide increases with the depth of the SLD potential well. Calculations using the theory of neutron channelling in planar waveguides predicted an exponential growth of the neutron channelling length with increasing SLD potential well depth.

The neutron channelling length was experimentally determined for the UP and DO polarization of the incident neutron beam for a sample magnetized to saturation and for the unpolarized incident beam for a fully demagnetized sample (non-magnetic or NM mode). The results showed that the neutron channelling length increases exponentially with the depth of the SLD potential well. Thus, the experimental results confirm the predictions of the neutron channelling theory in layered nanostructures.

ACKNOWLEDGMENTS

The authors thank T. Keller and F. Radu for useful discussions.

REFERENCES

1. *F. Ott*, *Focusing Optics for Neutrons*. In: Modern Developments in X-Ray and Neutron Optics. Springer Series in Optical Sciences. 2008. Vol. **137**. pp. 113–134.
2. *F. Ott, S. Kozhevnikov, A. Thiaville, J. Torrejon, M. Vazquez*, Nucl. Instrum. and Meth. A **788**, 29 (2015).
3. *F. Pfeiffer, V. Leiner, P. Høghøj, I. Anderson*, Phys. Rev. Lett. **88**, 055507 (2002).
4. *S. V. Kozhevnikov, A. Rühm, F. Ott, N. K. Pleshanov, J. Major*, Physica B **406**, 2463 (2011).
5. *S. V. Kozhevnikov, V. K. Ignatovich, Yu. V. Nikitenko, F. Ott, A. V. Petrenko*, JETP Letters **102**, 1 (2015).
6. *S. V. Kozhevnikov, V. D. Zhaketov, F. Radu*, JETP **127**, 593 (2018).
7. *S. V. Kozhevnikov, V. D. Zhaketov, T. Keller, Yu. N. Khaydukov, F. Ott, F. Radu*, Nucl. Instrum. and Meth. A **915**, 54 (2019).
8. *S. V. Kozhevnikov, F. Ott, J. Torrejón, M. Vázquez, A. Thiaville*, Phys. Solid State **56**, 57 (2014).
9. *F. Radu, V. K. Ignatovich*, Physica B **292**, 160 (2000).
10. *S. V. Kozhevnikov, V. K. Ignatovich, A. V. Petrenko, F. Radu*, JETP **123**, 950 (2016).
11. *Yu. V. Nikitenko*, Phys. Part. Nucl. **40**, 890 (2009).
12. *H. Zhang, P. D. Gallagher, S. K. Satija, R. M. Lindstrom, R. L. Paul, T. P. Russell, P. Lambooy, E. J. Kramer*, Phys. Rev. Lett. **72**, 3044 (1994).
13. *V. L. Aksenov, Yu. V. Nikitenko, F. Radu, Yu. M. Gledenov, P. V. Sedyshev*, Physica B **276–278**, 946 (2000).
14. *V. D. Zhaketov, K. Hramco, A. V. Petrenko, Yu. N. Khaydukov, A. Csik, Yu. N. Kopatch, N. A. Gundorin, Yu. V. Nikitenko, V. L. Aksenov*, Journal of Surface Investigation: X-ray, Synchrotron and Neutron Techniques **15**, 549 (2021).
15. *V. D. Zhaketov, A. V. Petrenko, S. N. Vdovichev, V. V. Travkin, A. Csik, Yu. N. Kopatch, Yu. M. Gledenov,*

E. Sansarbayar, N. A. Gundorin, Yu. V. Nikitenko, V. L. Aksenov, Journal of Surface Investigation: X-ray, Synchrotron and Neutron Techniques **13**, 478 (2019).

16. *Yu. V. Nikitenko, A. V. Petrenko, N. A. Gundorin, Yu. M. Gledenov, V. L. Aksenov*, Crystallogr. Rep. **60**, 466 (2015).

17. *V. L. Aksenov, V. D. Zhaketov, Yu. V. Nikitenko*. Phys. Part. Nucl. **54**, 756 (2023).

18. *V. L. Aksenov, Yu. V. Nikitenko, S. V. Kozhevnikov, F. Radu, R. Kruijs, T. Rekveldt*, Journal of Surface Investigation: X-ray, Synchrotron and Neutron Techniques **16**, 1225 (2001).

19. *Yu. Khaydukov, A. M. Petrzhik, I. V. Borisenko, A. Kalabukhov, D. Winkler, T. Keller, G. A. Ovsyannikov, B. Keimer*, Phys. Rev. B **96**, 165414 (2017).

20. *Yu. N. Khaydukov, D. Lenk, V. Zdravkov, R. Morari, T. Keller, A. S. Sidorenko, L. R. Tagirov, R. Tidecks, S. Horn, B. Keimer*, Phys. Rev. B **104**, 174445 (2021).

21. *M. Wolff, A. Devishvili, J. A. Dura, F. A. Adlmann, B. Kitchen, G. K. Pálsson, H. Palonen, B. B. Maranville, Ch. F. Majkrzak, B. P. Toperverg*, Phys. Rev. Lett. **123**, 016101 (2019).

22. *S. V. Kozhevnikov, F. Ott, E. Kentzinger, A. Paul*, Physica B **397**, 68 (2007).

23. *S. V. Kozhevnikov, F. Ott, A. Paul, L. Rosta*, Eur. Phys. J. Special Topics **167**, 87 (2009).

24. *E. Kentzinger, U. Rucker, B. Toperverg, T. Bruckel*, Physica B **335**, 89 (2003).

25. *F. Radu, A. Vorobiev, J. Major, H. Humblot, K. Westerholt, H. Zabel*, Physica B **335**, 63 (2003).

26. *L. Guasco, Y. N. Khaydukov, S. Pütter, L. Silvi, M. Paulin, T. Keller, B. Keimer*, Nature Communications **13**, 1486 (2022).

27. *A. Perrichon, A. Devishvili, K. Komander, G. K. Pálsson, A. Vorobiev, R. Lavén, M. Karlsson, M. Wolff*, Phys. Rev. B **103**, 235423 (2021).

28. *S. P. Pogossian, H. Le Gall, A. Menelle*, J. Magn. Magn. Mater. **152**, 305 (1996).

29. *S. V. Kozhevnikov, Yu. N. Khaydukov, T. Keller, F. Ott, F. Radu*, JETP Letters **103**, 36 (2016).

30. *S. V. Kozhevnikov, V. D. Zhaketov, T. Keller, Yu. N. Khaydukov, F. Ott, Chen Luo, Kai Chen, F. Radu*, Nucl. Instrum. and Meth. A **927**, 87 (2019).

31. *S. P. Pogossian*, J. Appl. Phys. **102**, 104501 (2007).

32. *V. K. Ignatovich, F. Radu*, Phys. Rev. B **64**, 205408 (2001).

33. *S. V. Kozhevnikov, T. Keller, Yu. N. Khaydukov, F. Ott, F. Radu*, Nucl. Instrum. and Meth. A **875**, 177 (2017).

34. *V. L. Aksenov, Yu. V. Nikitenko*, Physica B **297**, 101 (2001).

35. *S. V. Kozhevnikov, V. K. Ignatovich, F. Ott, A. Rühm, J. Major*, JETP **117**, 636 (2013).

36. *Yu. V. Nikitenko, V. V. Proglyado, V. L. Aksenov*, Journal of Surface Investigation: X-ray, Synchrotron and Neutron Techniques **8**, 961 (2014).

37. S. V. Kozhevnikov. Phys. Particl. Nucl. **50**, 300 (2019).

38. *S. V. Kozhevnikov, V. D. Zhaketov, Yu. N. Khaydukov, F. Ott, F. Radu*, JETP **125**, 1015 (2017).

39. *S. V. Kozhevnikov, T. Keller, Yu. N. Khaydukov, F. Ott, F. Radu*, JETP **128**, 504 (2019).

40. *S. V. Kozhevnikov, Yu. N. Khaydukov, F. Ott, F. Radu*, JETP **126**, 592 (2018).

41. *Yu. N. Khaydukov, O. Soltwedel, T. Keller*, J. Large Scale Research Facilities A **38**, 1–4 (2015).

42. *S. V. Kozhevnikov, A. Rühm, J. Major*, Crystallography Reports **56**, 1207 (2011).